Nanoscale

PAPER

View Article Online
View Journal | View Issue

Cite this: *Nanoscale*, 2024, **16**, 13050

A hydrogel based on Fe(II)-GMP demonstrates tunable emission, self-healing mechanical strength and Fenton chemistry-mediated notable antibacterial properties†

Umesh, ‡[a] Vysakh C. Chandran,‡[a] Pranay Saha, [b] Debasish Nath,[a] Sayan Bera,[b] Santanu Bhattacharya *[b,c] and Asish Pal *[a]

Received 10th March 2024,
Accepted 6th June 2024

DOI: 10.1039/d4nr01011f

rsc.li/nanoscale

Supramolecular hydrogels serve as an excellent platform to enable *in situ* reactive oxygen species (ROS) generation while maintaining controlled localized conditions, thereby mitigating cytotoxicity. Herein, we demonstrate hydrogel formation using guanosine-5′-monophosphate (GMP) with tetra(4-carboxylphenyl) ethylene (**1**) to exhibit aggregation-induced emission (AIE) and tunable mechanical strength in the presence of divalent metal ions such as Ca^{2+}, Mg^{2+}, and Fe^{2+}. The addition of divalent metal ions leads to structural transformation in the metallogels (**M-1$_{GMP}$**). Furthermore, the incorporation of Fe^{2+} ions into the hydrogel (**Fe-1$_{GMP}$**) promotes the Fenton reaction that could be upregulated upon adding ascorbic acid (**AA**), demonstrating antibacterial efficacy *via* ROS generation. *In vitro* studies on **AA**-loaded **Fe-1$_{GMP}$** demonstrate excellent bacterial killing efficacy against *E. coli*, *S. aureus* and vancomycin-resistant enterococci (VRE) strains. Finally, *in vivo* studies involving topical administration of **Fe-1$_{GMP}$** to Balb/c mice with skin infections further suggest the potential antibacterial efficacy of the hydrogel. Taken together, the hydrogel with its unique combination of mechanical tunability, ROS generation capability and antibacterial efficacy can be used for biomedical applications, particularly in wound healing and infection control.

Introduction

Bacterial infections have far-reaching consequences for global health, constituting a significant burden on healthcare systems and necessitating continuous efforts in research and treatment.[1] The predominant approach in the therapeutic management of bacterial infections has so far been through antibiotic treatment. Yet, the irrational and rampant use of antibiotics is leading to the threat of antimicrobial resistance (AMR) due to the bacteria developing self-mechanisms to resist the action of these pharmacological agents.[2,3] Of late, there has been an upsurge in the development of alternative and effective treatment strategies to mitigate such threats.[4] In this regard, hydrogels have evolved as promising candidates to mitigate bacterial infections, especially in wound healing, tissue engineering and other disease conditions.[5–9] These nanostructured materials can possess inherent antibacterial activity or can be utilized toward the targeted and controlled release of antimicrobial drugs, enhancing both specificity and potency in combating bacterial infections.[10–15] Moreover, hydrogels due to their cargo loading efficacy, mechanical strength, response to different stimuli and wettability have evolved as a primary tool to be employed in various strategies of microbial management.[15] These strategies include loading antibacterial drugs into hydrogels for controlled release at infected sites, utilizing active antibacterial agents as gelators that can form gels through interactions with other molecules and developing hydrogels capable of exhibiting photothermal therapy (PTT) or photodynamic therapy (PDT).[16–18]

Recently, such biomaterials and hydrogels have been developed for the prevention of bacterial infections in wound healing while addressing challenges of AMR.[19–21] Such hydrogels primarily act as carrier systems for delivering antimicrobial agents or as templates for ROS production to control bacterial infections. Through the localized delivery of antibiotics or ROS, hydrogels minimize the exposure of bacteria to the sublethal concentrations of these agents in a bid to mitigate the development of bacterial resistance. Therefore, hydro-

[a]*Chemical Biology Unit, Institute of Nano Science and Technology, Knowledge City, Sector 81, Mohali, Punjab 140306, India. E-mail: apal@inst.ac.in*
[b]*School of Applied & Interdisciplinary Sciences, Indian Association for the Cultivation of Science, Kolkata, 700032, India. E-mail: sb23in@yahoo.com*
[c]*Department of Chemistry, Indian Institute of Science Education and Research Tirupati, Yerpedu Mandal, Tirupati District, Andhra Pradesh, 517619, India*
†Electronic supplementary information (ESI) available: Synthesis and additional figures. See DOI: https://doi.org/10.1039/d4nr01011f
‡These authors contributed equally to this work.

gels offer a promising approach for combating bacterial infections while minimizing the risk of resistance development. Haldar *et al.* developed a polymeric hydrogel-based wound dressing that shows a broad spectrum of bactericidal activities and potent wound healing capability.[22] In another approach, Bajaj *et al.* developed a cholic acid-derived non-immunogenic supramolecular hydrogel for the treatment of *Staphylococcus aureus* infections in topical wounds.[23] Recently, peptide-based hydrogels showed great promise as potential antimicrobial and antibiofilm agents to address chronic wound healing owing to the presence of charged amino acids, *e.g.* arginine and lysine, and conjugation of anti-inflammatory drugs.[24–27] In another strategy, Chatterjee *et al.* have reported the effect of the hydrophobic side chain length of peptides on antibacterial activity and cytotoxicity.[28] Stupp *et al.* reported self-assembled peptide nanofiber-anchored silver nanoparticles in organic–inorganic hybrids to exhibit robust antimicrobial properties.[29]

Recently, we also reported a strategy to mitigate bacterial multidrug resistance by forming a charge transfer complex between the donor–acceptor pair of peptide-tethered pyrene and tetracyanoquinodimethane to inhibit bacterial growth owing to its high charge mobility to perturb the electrochemical potential of bacterial cell membranes.[30] In this regard, PDT has emerged as a targeted and minimally invasive approach with fewer side effects and high cure rates in the treatment of certain types of cancer, skin diseases and microbial infections.[31,32] This involves a photosensitizing agent that absorbs light and generates ROS to stimulate oxidative stress and ultimately trigger a cascade of events leading to cell death. Reactive oxygen species include the superoxide anion ($O_2^{\bullet-}$), singlet oxygen ($^1O_2$) and the hydroxyl radical ($^{\bullet}OH$). Srivastava *et al.* reported temporal ROS generation in phenylalanine self-assembled hydrogel composites for anticancer applications.[33] Recently, Zheng *et al.* showcased antibacterial PDT by generating $^1O_2$ using a boron dipyrromethene photosensitizer.[34] Such ROS generation can also be mitigated by multiple chemical reactions such as oxidative phosphorylation, NADPH oxidases, the heme oxygenase reaction and the Fenton reaction.[35] The Fenton reaction is a chemical reaction involving the generation of ROS, specifically hydroxyl radicals, through the interaction of hydrogen peroxide (H_2O_2) with Fe^{2+} ions.[36] The amount of H_2O_2 available for oxidation may also account for the production of $^{\bullet}OH$.[37] Harnessing the Fenton reaction to address microbial contamination holds promise for diverse applications, including water decontamination and the formulation of antimicrobial coatings.[38,39]

However, challenges, such as the need for controlled ROS generation with minimal H_2O_2 usage and considerations of cytotoxicity, must be addressed to mitigate microbial infections.

Thus, achieving precise spatiotemporal control over ROS generation is crucial for achieving their biomedical application.[40] Supramolecular hydrogels,[41–43] especially metallogels, offer an ideal platform for this purpose, providing a biologically relevant and adjustable nanostructure capable of accommodating the Fenton reaction. Shen *et al.* reported photothermally enhanced $^{\bullet}OH$ radical production towards crosslinking hydrogels and subsequent bacteria-infected diabetic wound management.[44] However, a rational control over the crosslinking of hydrogels for hosting such a Fenton reaction is rather limited. This prompted us to develop biocompatible supramolecular hydrogels with tuneable architectures and properties for ROS generation.

Herein, we envisaged guanosine monophosphate (GMP)-based hydrogels as driven by the extensive Hoogsteen-type hydrogen bonding among the guanosine nucleobases to facilitate metal ion stabilized G-quadruplex self-assembled structures.[45,46] Herein, we demonstrate additional hydrogen bonding interactions of a GMP-based G-quadruplex with tetravalent tetra(4-carboxylphenyl) ethylene (**1**) to generate a $\mathbf{1_{GMP}}$ hydrogel (Scheme 1). Such additional cross-linking presumably reinforces the G-quadruplex secondary structures to form hydrogels and exhibit AIE behavior. Interestingly, upon binding with divalent metal ions, the change in secondary structures modulates the AIE and increases the mechanical strength of the resulting metallogels ($\mathbf{M\text{-}1_{GMP}}$). Furthermore, we exploited the $\mathbf{Fe\text{-}1_{GMP}}$ hydrogel for *in situ* ROS generation using the Fenton reaction in the presence of H_2O_2, which was upregulated upon addition of ascorbic acid (**AA**). To our knowledge, hosting the Fenton reaction in metallogels for controlled evolution of ROS has so far not been attempted. We showed efficient antibacterial efficacy against *E. coli*, *S. aureus* and vancomycin-resistant enterococci (VRE) mediated by ROS generation in the $\mathbf{Fe\text{-}1_{GMP}}$ hydrogel. Finally, we validated the antibacterial efficacy of the hydrogel hosting Fenton reaction against *E. coli* in an *in vivo* Balb/C mouse model.

Experimental section

Preparation of the hydrogel ($\mathbf{1_{GMP}}$)

A powdered form of GMP (12 mg) was taken in 500 μL of 60 mM acetate buffer at pH 4 and heated to complete dissolution to obtain a GMP (60 mM) solution of pH 4. Subsequently, various concentrations (1 mM to 9 mm) of tetra (4-carboxylphenyl) ethylene (**1**) in ethanol was added to the GMP solution, followed by heating at 80 °C for 10 min and then gradual cooling which ensued gelation. We noticed that only an optimum concentration range of **1** (4.5 to 6 mM) furnished strong hydrogels of $\mathbf{1_{GMP}}$.

For the preparation of metallogels ($\mathbf{M\text{-}1_{GMP}}$), divalent metal salt solutions of Ca^{2+}, Mg^{2+}, and Fe^{2+} (1 mM) were added to the hot solution of $\mathbf{1_{GMP}}$ at 70 °C, followed by subsequent gradual cooling to room temperature. The metallogel formation was optimized by varying the ratio of metal ions w.r.t. $\mathbf{1_{GMP}}$.

Spectral studies of the hydrogels

The samples were prepared by drop-coating 100 μL of the hydrogel on a quartz slide for circular dichroism and fluorescence spectral studies. Fluorescence spectra were recorded with an Edinburgh Instruments spectrofluorometer FS5.

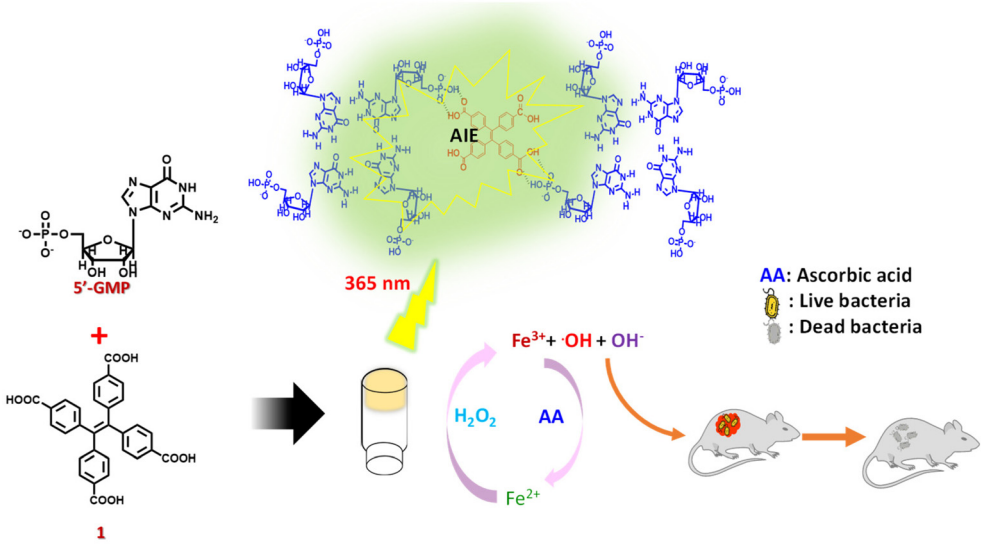

Scheme 1 Supramolecular hydrogels mediated by the crosslinking of GMP with **1** and divalent metal ions (**M**) as in **M-1$_{GMP}$** to exhibit aggregation-induced emission. The **Fe-1$_{GMP}$** hydrogel exhibits upregulation of the Fenton reaction in the presence ascorbic acid to generate ROS for eventual application in controlling bacterial growth in topical wounds.

Circular Dichroism (CD) spectra were recorded using a JASCO J-1500 circular dichroism spectrometer from Easton, MD, USA. Samples for ^{1}H-NMR analysis were prepared from the lyophilized hydrogel powder after suspending it in D_2O and ^{1}H-NMR spectra were recorded using an FT-NMR Bruker 400 MHz NMR spectrometer.

Rheology of the hydrogels

Rheological assessments were carried out using an Anton Paar rheometer MCR302 device equipped with Rheocompass version 1.31 software and a cone plate (CP-25) configuration featuring a controllable Peltier system. The measurements were performed with a 0.2 mm gap distance.

ROS generation

The **Fe-1$_{GMP}$** hydrogel (0.6 mM) was taken with and without **AA** in 1000 μL of acetate buffer at pH 4. Methylene blue (MB) solution (0.1 mM) in water was added to record the UV-visible absorption spectra. Furthermore, H_2O_2 was gradually added (ranging from 0.05 mM to 50 mM) to monitor the reduction in the intensity of absorbance due to MB. The percentage degradation of dye was calculated by taking the absorbance of the hydrogel with MB before adding H_2O_2 as 100%.

In vitro antimicrobial studies

Antimicrobial properties were evaluated against the strains of bacteria, *E. coli* and *S. aureus* that were grown overnight in Luria–Bertani (LB) at 37 °C to a final bacterial concentration of 3×10^6 CFU mL^{-1}. For drug-resistant bacterial strain, *Enterococcus faecium* was grown in brain heart infusion broth (BHIB) media at 37 °C to a final concentration of 5×10^6 CFU mL^{-1}. Then, 100 μL of the bacterial stock was suspended in 2 mL of the corresponding medium. The hydrogels were sterilized under UV light. In the test samples, **H_2O_2** was injected just before adding the hydrogels to the media containing bacteria. A control with only **H_2O_2** was also taken for comparison. The treated samples were kept in a BOD incubator at 37 °C and thoroughly shaken for 16 h. Then, 100 μL of suspension was taken as an aliquot from each sample and diluted accordingly using autoclave water. Furthermore, 100 μL of this diluted suspension was spread on the LB agar, BHI agar plates were incubated at 37 °C for another 14 h before taking the agar plates for visualizing bacterial colonies. For comparison, the microbial assay was conducted taking silver sulfadiazine as a standard. Furthermore, for quantification, colony forming units per mL (c.f.u per mL) of bacterial cells was calculated.

Cellular compatibility of the hydrogels

The biocompatibility and cellular proliferation ability of the hydrogels (**Fe-1$_{GMP}$** and **Fe-1$_{GMP}$ + AA**) were assessed using mouse fibroblast L929 cell lines in a cytotoxicity assay. The cells were individually cultured in Dulbecco's Modified Eagle's Medium (DMEM, Cytiva) supplemented with 10% fetal bovine serum (FBS) (Gibco, Thermo Fisher Scientific) at 37 °C and 5% CO_2. Culturing was performed in 25 cm cell culture flasks from Cole-Parmer and the cells were passaged upon reaching 60–70% confluency. Biocompatibility tests with different concentrations of **Fe-1$_{GMP}$** and **Fe-1$_{GMP}$ + AA** were performed using 3-(4,5-dimethylthiazol-2-yl)-2,5-diphenyltetrazolium bromide in the MTT assay. 5000 L929 cells per well were seeded with DMEM (HIMEDIA) supplemented with 10% FBS in a 96-well plate. After overnight incubation, different concentrations of the media containing **Fe-1$_{GMP}$** and **Fe-1$_{GMP}$ + AA** were treated for 48 h at 37 °C, followed by the addition of MTT at a concentration of 0.5 mg mL^{-1} and incubated for 2 h. The absorbance of DMSO-solubilized formazan crystals was measured at

570 nm using a BIOTEK multiplate reader. The assay was performed in triplicate for each sample.

In vivo antimicrobial study on rat skin

Animal experiments, approved by the Institutional Animal Ethics Committee, were conducted following the ethical guidelines (no. IACS/IAEC/2018/04). For the *in vivo* study, male Balb/c mice aged around 6–8 weeks and weighing 20–25 g were chosen. These mice were procured from the National Institute of Nutrition (NIN) animal facility in Hyderabad. Neutropenia was induced in all mice by dual administration of cyclophosphamide monohydrate (TCI chemicals) *via* intraperitoneal injection with both doses given at a concentration of 100 mg per kg body weight (the second dose was administered 3 days after the first). After 24 hours from the second dose, the mice were taken out and the hair around the dorsal midline was trimmed and removed using hair removal cream. The region was then made aseptic by rubbing with 70% ethanol. For the study, a pathogenic strain of *E. coli* was prepared following the LB broth method. The bacterial solution was incubated overnight. After centrifugation, the bacterial pellet was dissolved in sterile 1× PBS buffer (100 μL).

Furthermore, dorsal surfaces of the mice were mildly wounded to create a skin abrasion. The bacterial solution (100 μL) was added to this surface and secured with a sterile gauge and band-aids on all sides to allow aeration for the inoculated bacterial biomass to colonize the skin and form biofilms. After 24 hours of undisturbed incubation, the hydrogel formulations (four different sets: $\mathbf{1_{GMP}}$ without **AA**, only $\mathbf{H_2O_2}$, $\mathbf{1_{GMP}}$ without **AA** and $\mathbf{H_2O_2}$, and $\mathbf{1_{GMP}}$ with **AA** and $\mathbf{H_2O_2}$) were applied on mouse skin. After 24 hours, the mice were sacrificed and the dorsal skin portions were isolated and washed with 0.9% NaCl to remove residual bacteria and gel particles.

A portion of the skin was homogenized and the bacterial biomass was dislodged. The resulting solution was centrifuged and the dislodged bacteria were obtained. The supernatant was used to determine the number of colony-forming units (CFU) per 50 mg of skin tissue. Equal volumes from each group were diluted, plated on nutrient agar and incubated at 37 °C in a BOD incubator overnight and the colonies were observed.

Another fraction of the mouse skin was homogenized and the displaced bacterial population was subjected to centrifugation using a REMI C24 plus centrifugation machine at 5000 rpm. The bacteria were stained to quantify live and dead cells employing Syto-9 (Invitrogen™ SYTO™ 9 green fluorescent nucleic acid stain) and propidium iodide (PI) (Sigma-Aldrich) in a 1 : 1 staining mixture. The concentrations of the two dyes were set at 5 μM for Syto-9 and 30 μM for propidium iodide, both prepared in 1× PBS buffer. The bacterial pellet obtained from centrifugation was dissolved in 50 μL of 1× PBS buffer containing the dyes and left to incubate in the dark for 20 min. Then a solution inoculum was placed on a clean sterile glass slide, covered with a coverslip, and kept at 4 °C for 30 minutes. Fluorescence images of the bacterial biomass were captured using an EVOS M5000 imaging system.

Results and discussion

G-quartet hydrogel formation

Guanosine 5′-monophosphate disodium salt self-assembled in acetate buffer of pH 4 into a viscous solution, presumably due to the formation G4-quartet structures as mediated by the hydrogen bonding donor–acceptor pair in guanosine bases that was further stabilized by sodium ions for G-quadruplex structures.[47] However, even after repeated annealing, it did not form hydrogels, indicating the weak nature of crosslinking. Interestingly, upon addition of an ethanolic solution of tetra(4-carboxylphenyl) ethylene (**1**) with four carboxylic acid motifs, we observed the formation of hydrogels at an optimal concentration.[48] Introduction of **1** promotes the cross-linking among the G4-quartet stacks *via* hydrogen bonding interactions. Each G4-quartet unit contains four phosphoric groups, while **1** possesses four carboxylic acid groups available for hydrogen bonding. This suggests the significance of the stoichiometry between the two components in the gelation process. To investigate this, gelation experiments were conducted by varying the concentration of **1**, ranging from 1 mM to 9 mM (Fig. 1A). Gelation was specifically observed at 4.5 mM and 6 mM concentrations of **1**. However, precipitation of **1** occurred at higher concentrations, presumably due to its limited solubility in the aqueous medium. Notably, gelation did not occur at the lower concentration of **1**, indicating insufficient cross-linking to underscore the critical role of the **1** and GMP ratio in gelation. The self-assembly mechanism was further investigated through comparative ^{1}H-NMR studies (Fig. 1B). The addition of **1** to the GMP solution in D_2O resulted in a downfield shift in the proton peak (a) adjacent to the phosphate group from δ = 3.99 to 4.10 ppm which suggested the active involvement of the phosphate group in hydrogel formation through hydrogen bonding. Additionally, a downfield shift was observed in the aromatic proton peak (b′) of **1** (Fig. S1†) to provide additional confirmation for the involvement of the COOH group in hydrogen bonding interactions. Similarly, we observed a shift in the ^{1}H-NMR peaks of the protons (a, b, c, and d) from the pentose sugar upon binding to **1**. This suggested the presence of an extensive H-bonding network among the carboxylic moieties of **1** and the phosphoric groups of G4-quadruplex structures to provide additional crosslinking, leading to the formation of the $\mathbf{1_{GMP}}$ hydrogel. Furthermore, the hydrogel exhibited green emission under UV light at a wavelength of 365 nm attributable to the aggregation-induced emission (AIE) properties of **1** (Fig. 1C). The CD spectra of $\mathbf{1_{GMP}}$ exhibited negative Cotton bands at 216 and 279 nm and a positive Cotton band at 315 nm (Fig. 1D), indicating the presence of G4-quadruplex secondary structures mediated by H-bonding as corroborated from ^{1}H-NMR. Next, the comparative mechanical properties of the hydrogels formed at different concentrations of **1** were investigated by rheological studies. The oscillatory frequency

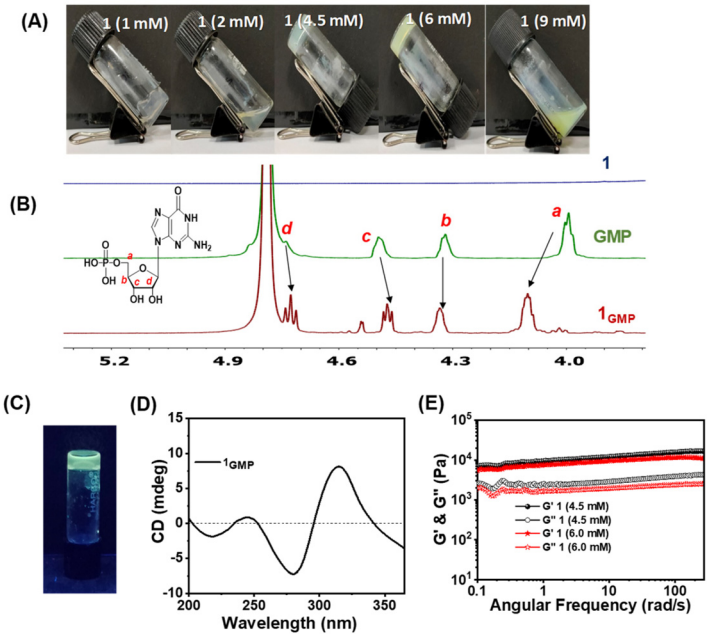

Fig. 1 (A) Digital images of hydrogel formation at different concentrations of **1** and 60 mM **GMP**. (B) Comparative ^{1}H-NMR spectra of **1** in DMSO-d_6 and **GMP** and $\mathbf{1_{GMP}}$ in D_2O, showing shifts in the peak position of the pentose sugar ring protons upon hydrogel formation. (C) Digital image of the $\mathbf{1_{GMP}}$ hydrogel showing AIE under UV light (365 nm). (D) CD spectra of $\mathbf{1_{GMP}}$ showing positive and negative CD signals, confirming the presence of the G4-quadruplex stacks of GMP. (E) Frequency sweep rheological measurements of $\mathbf{1_{GMP}}$ at different concentrations of **1**.

sweep experiment for hydrogel networks exhibited a frequency-independent behaviour over three orders of angular frequency with a G' value of ~1000 Pa and a G'/G'' ratio of ~4 (Fig. 1E) to indicate mechanically stiff and viscoelastic solid-like hydrogels for $\mathbf{1_{GMP}}$.

Effect of metal ions in the metallogel

Next, we investigated the impact of divalent metal ions on the self-assembling properties of $\mathbf{1_{GMP}}$. Thus, 1 mM calcium (Ca^{2+}), iron (Fe^{2+}) and magnesium (Mg^{2+}) were added to $\mathbf{1_{GMP}}$ (60 mM). Interestingly, the hydrogel structures remained intact even after the addition of these divalent metal ions. Upon adding Ca^{2+}, Mg^{2+} and Fe^{2+} to $\mathbf{1_{GMP}}$, we observed an increase in absorbance in the ~350 nm wavelength range in the UV-Vis spectra (Fig. S2A†). Notably, all the samples in the vial exhibited strong emission behavior under UV_A (λ_{max} = 365 nm) light (Fig. 2A inset). Furthermore, we employed fluorescence spectroscopy to investigate the role of **1** in the emission behavior of the hydrogels as compared to its monomeric state (Fig. S2B†). Thus, we observed a significant increase in the emission intensity of $\mathbf{1_{GMP}}$ hydrogels at 510 nm that could be attributed to the aggregation-induced emission (AIE) properties of **1**. Moreover, increased crosslinking with metals for $\mathbf{M\text{-}1_{GMP}}$ metallogels led to a further increase in the emission intensity, possibly due to the stabilization of higher order aggregated states by different metal ions (Fig. 2A). The trend of emission intensity with $\mathbf{Ca\text{-}1_{GMP}} < \mathbf{Mg\text{-}1_{GMP}} < \mathbf{Fe\text{-}1_{GMP}}$ hydrogels is worth noting. Next, we subjected the $\mathbf{Fe\text{-}1_{GMP}}$ hydrogel for heat–cool cycles to achieve reversible gel-sol-gel transition. Interestingly, the hydrogel exhibited reversible AIE behaviour as monitored at 510 nm with a noticeable increase in the emission intensity upon gel formation that was subsequently diminished upon heating (Fig. 2B). Furthermore, we recorded CD spectra to assess the alterations in the secondary structure of $\mathbf{1_{GMP}}$ induced by the addition of metal ions (Fig. 2C). $\mathbf{1_{GMP}}$ exhibited the characteristic CD signature of G-quadruplex; however, upon the addition of Mg^{2+} and Ca^{2+}, we observed negative Cotton bands at 240 and 325 nm and a positive Cotton band at 265 nm. This clearly indicated the transformation of the G-quadruplex structures to G-triplex stacks as reported in the literature.[48,49] In contrast, in the presence of Fe^{2+}, no characteristic CD signals were observed, implying the absence of G-quartet or G-triplex stacks in the formed nanostructures.

This was further corroborated by PXRD where the peak at 2θ = 27.5° corresponding to G4-quadruplex stacking among the two adjacent vertical G–G stacks was absent for the case of the Fe^{2+} ion, hence indicating the absence of prominent G4-quadruplex stacks (Fig. S2C†).[50] To further investigate the intricacies of the self-assembly mechanism, we performed ^{1}H-NMR spectral analysis that highlighted the distinct characteristics of the protons in $\mathbf{Fe\text{-}1_{GMP}}$ compared to other metallogels ($\mathbf{M\text{-}1_{GMP}}$) (Fig. 2D and E). Thus, the protons from the nucleobase (f) and the pentose sugar (e) peaks display a downfield shift and a broadening for $\mathbf{Fe\text{-}1_{GMP}}$ in the case of $\mathbf{Fe\text{-}1_{GMP}}$, suggesting the coordination of Fe^{2+} ions with the nucleobase group (Scheme 2). Additionally, the aromatic proton peak (b′) of **1** showed a slight upfield shift in $\mathbf{Fe\text{-}1_{GMP}}$, indicating the potential involvement of molecule **1** in facilitating the self-

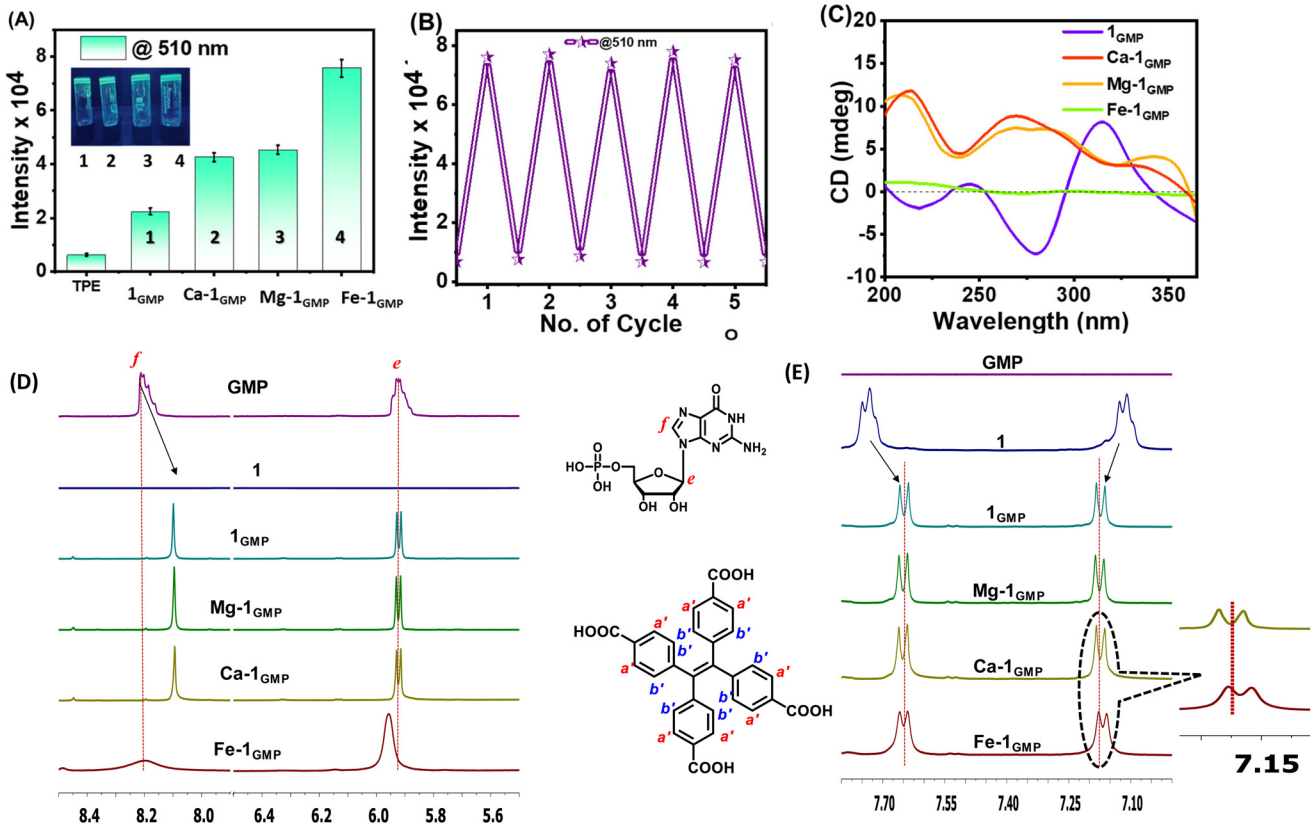

Fig. 2 (A) Fluorescence spectroscopy exhibiting the change in the emission intensity of **1** in the hydrogels formed with different metal ions. Inset: a digital image of the hydrogels with various metal ions under UV light (365 nm). (B) Fluorescence emission of **Fe-1$_{GMP}$** with the heating–cooling cycle showing reversible gel to sol conversion. (C) Comparison of the CD spectra of metallogels showing structural transitions from G-quadruplex structures. (D and E) Comparative ^{1}H-NMR spectra of the **M-1$_{GMP}$** hydrogels with different metal ions in D_2O in different chemical shift ranges characteristic of the protons of GMP and **1**.

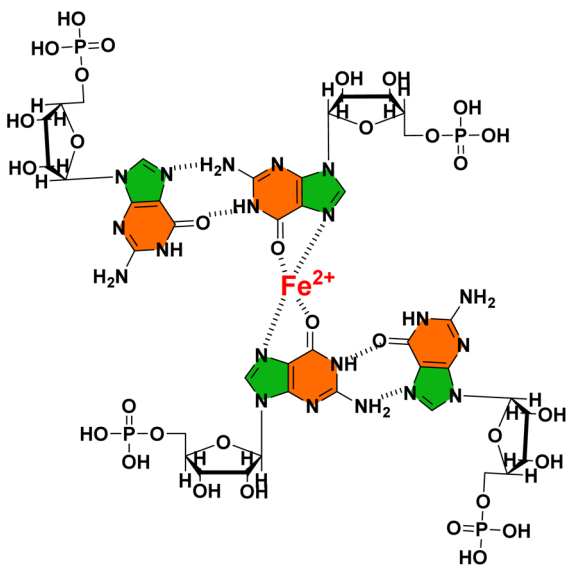

Scheme 2 Schematic illustration of the possible interaction of Fe^{2+} with 5′-GMP in the **Fe-1$_{GMP}$** hydrogel.

assembly process. Furthermore, the pentose ring protons exhibited a broader nature in **Fe-1$_{GMP}$** (Fig. S2D†), suggesting the absence of G4-quadruplex stacks within the **Fe-1$_{GMP}$** assembly as corroborated from the observations of the CD spectral and PXRD data. FE-SEM showed the presence of a nano-fibrillar network of the **Fe-1$_{GMP}$** hydrogel network (Fig. S2E†).

Tunable mechanical strength in metallogels (M-1$_{GMP}$)

Next, we compared the bulk mechanical properties of the metallogels (**M-1$_{GMP}$**) using frequency sweep oscillatory rheological studies (Fig. 3A). As compared to the native **1$_{GMP}$** hydrogel, all the metallogels showed higher G' values and frequency-independent behaviour, indicating the reinforced mechanical strength upon adding divalent ions. However, no gel formation was observed when GMP and **1** were individually mixed with the metal ions (Fig. S3A†). We noted the following trend with the increase of storage moduli (G'): **1$_{GMP}$** < **Ca-1$_{GMP}$** < **Fe-1$_{GMP}$** < **Mg-1$_{GMP}$** (Fig. 3B). We further varied the concentration of Fe^{2+} to optimize the metal ion : **1$_{GMP}$** ratio to improve the strength of the **Fe-1$_{GMP}$** hydrogel. We performed frequency sweep oscillatory measurement on the hydrogels for varied concentrations of Fe^{2+} (Fig. 3C) and found a maximum

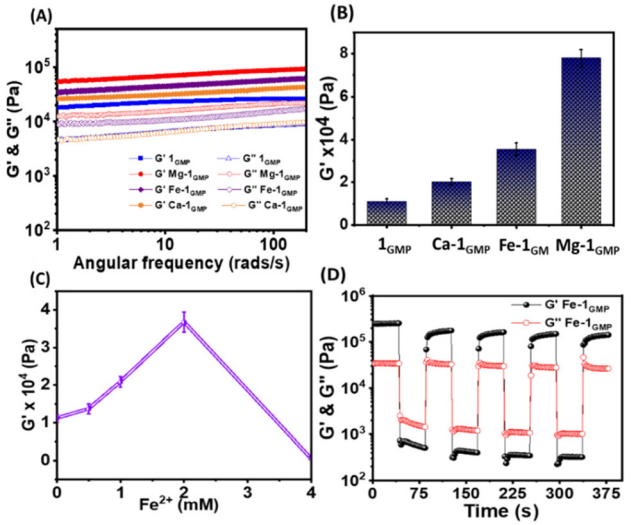

Fig. 3 (A) Frequency sweep oscillatory rheology for the **M-1$_{GMP}$** metallogels and the native **1$_{GMP}$** hydrogel and (B) the corresponding bar diagram showing storage moduli, *G'*, upon addition of different metal ions. (C) Storage moduli of **Fe-1$_{GMP}$** with varying concentrations of the Fe^{2+} ion. (D) Dynamic thixotropy study of the **Fe-1$_{GMP}$** hydrogel performed at a constant angular frequency of 5 rad s^{-1} and a temperature of 25 °C with alternating low and high strains of 0.1 and 100%, respectively.

mechanical strength attained at a concentration of 2 mM Fe^{2+} with **GMP** (60 mM) and **1** (4.5 mM). We investigated the reversibility of the **Fe-1$_{GMP}$** hydrogel by subjecting the hydrogel to five consecutive heat–cool cycles. Thus, the gel was heated to 70 °C to convert it into a sol state, followed by sonication for 2 min and gradual cooling at room temperature. We noticed consistent hydrogel formation within 3–5 min after each cycle, confirming the reversible nature of **Fe-1$_{GMP}$** (Fig. S3B†). Next, we subjected the **Fe-1$_{GMP}$** hydrogel to dynamic thixotropic studies involving alternating cycles of high deforming shear (strain 200% at 5 rad s^{-1}), followed by recovery (strain 1% at 5 rad s^{-1}). The **Fe-1$_{GMP}$** hydrogel exhibited 94% recovery, confirming its self-healing behavior (Fig. 3D).[51–53] Thus, combining such a mechanical response of the **Fe-1$_{GMP}$** hydrogel with the multiple oxidation states of Fe, this hydrogel emerged as a promising candidate to host the Fenton chemistry in a controllable manner.

ROS generation *via* the Fenton reaction

It occurred to us that the metallohydrogels (**M-1$_{GMP}$**) with **M** in multiple oxidation states could participate in the Fenton reaction, albeit in a diffusion-controlled manner in the hydrogel. Thus, we explored the **Fe-1$_{GMP}$** hydrogel's ability to trigger the Fenton reaction to generate reactive oxygen species, *e.g.* hydroxyl radicals (˙OH) that might have potential antibacterial properties (Fig. 4A). In the Fenton reaction, Fe^{2+} in the hydrogel might get oxidized to Fe^{3+} by H_2O_2 to generate a hydroxyl radical and an anion. We probed such ˙OH generation in a dye degradation experiment by monitoring the characteristic absorbance of methylene blue (**MB**) dye at 667 nm in the UV-visible spectra. MB dye was added to the **Fe-1$_{GMP}$** hydrogel;

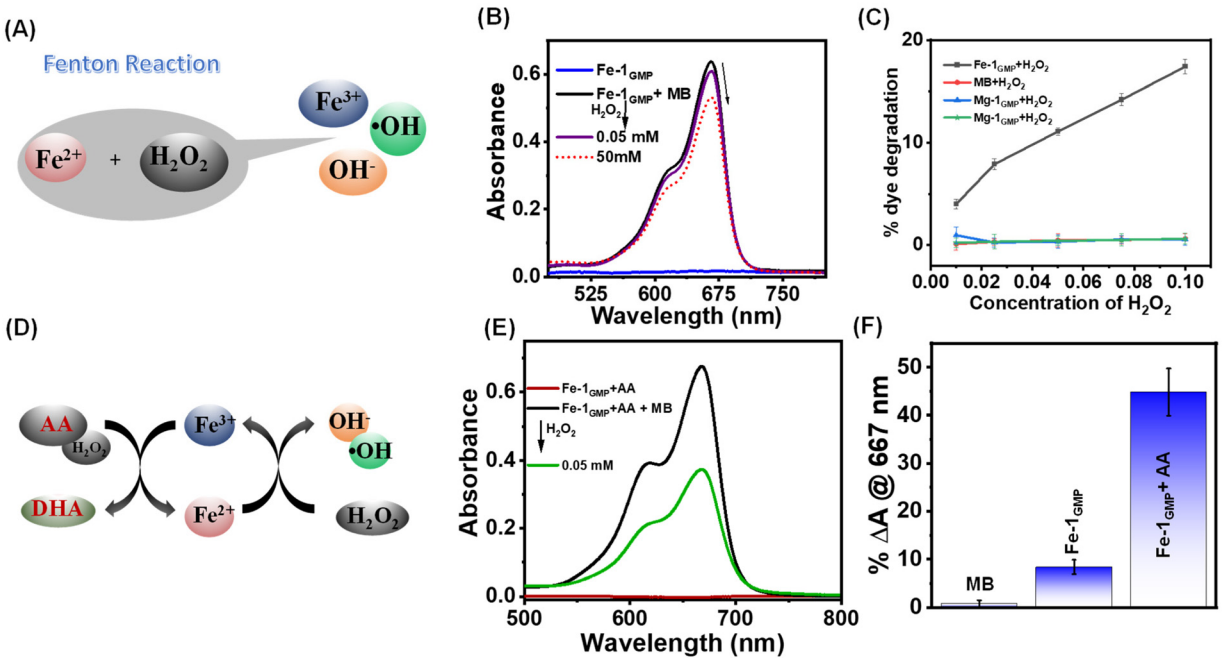

Fig. 4 (A) Schematic representation of the Fenton reaction illustrating the conversion of ferrous ions (Fe^{2+}) and hydrogen peroxide (H_2O_2) into ferric ions (Fe^{3+}), hydroxyl radicals (˙OH), and hydroxide ions (OH^-). (B) UV-vis spectra depicting changes in the absorption of the **MB** dye following successive additions of H_2O_2 solution to **Fe-1$_{GMP}$**. (C) Comparison with respect to dye degradation in different hydrogels. (D) Schematic illustration of the role of ascorbic acid in increasing the production of reactive oxygen species (ROS). (E) UV-vis spectra showing enhanced degradation of MB after the addition of **AA** to **Fe-1$_{GMP}$**. (F) Comparison of the percentage dye degradation of **Fe-1$_{GMP}$** and **Fe-1$_{GMP}$** + **AA** by addition of 0.05 mM H_2O_2.

however, gradual addition of H_2O_2 solution in the concentration range of 0.05 mM–50 mM in **Fe-1$_{GMP}$** exhibited a decrease in the dye absorbance (Fig. 4B and S4A†). Such reduction in the absorbance indicated the degradation of MB dye, signifying *in situ* generation of ROS mediated by the Fenton reaction within **Fe-1$_{GMP}$** (Fig. 4C). A control study performed to show the stability of the **MB** dye in the presence of only **H_2O_2** without the **Fe-1$_{GMP}$** hydrogel clearly confirmed the specificity of ROS generation (Fig. S4B†). Moreover, we did not observe such ROS generation in other metallogels, **M-1$_{GMP}$** with Ca^{2+} and Mg^{2+} that indicated the significant of Fe^{2+} in the network (Fig. S4C and D†). Furthermore, in a bid to ramp up the ROS generation, we incorporated 10 mM ascorbic acid (**AA**, $C_6H_8O_6$) in the **Fe-1$_{GMP}$** hydrogel network. Addition of **AA** did not affect the hydrogel formation and mechanical properties of the hydrogels as shown by the rheological studies for both **Fe-1$_{GMP}$** and **Fe-1$_{GMP}$** + **AA** with G' values of ~20 kPa (Fig. S5A and B†). Ascorbic acid played a crucial role in the reduction of Fe^{3+} (ferric iron) to Fe^{2+} (ferrous iron), resulting in the conversion and promoting the production of ROS. The oxidized form of ascorbic acid, dehydroascorbic acid (DHA), was produced as a result of the redox reaction after the addition of **H_2O_2** (Fig. 4D). We monitored the ROS generation and **MB** degradation using UV-vis spectra with a significant decrease in the absorbance upon addition of a low concentration (0.05 mM) of **H_2O_2** (Fig. 4E).

Thus, **Fe-1$_{GMP}$** alone exhibited only 10% dye degradation while **Fe-1$_{GMP}$** with ascorbic acid showed 45% of dye degradation with the same H_2O_2 concentration (Fig. 4F). The control **MB** dye with H_2O_2 showed only 1% degradation of the dye that suggested the significantly enhanced efficacy of ROS generation in the presence of **AA** within the **Fe-1$_{GMP}$** system. Interestingly, the formation of Fe^{3+} resulted in the weakening of the gel, as observed from the rheological studies (Fig. S5C†). A substantial decrease in the storage modulus (G') value was observed, decreasing from 35 kPa to 7.7 kPa that was even lower than the G' value of the gel without the addition of ions (11.1 kPa). This suggested that the mechanical strength of the hydrogel decreased significantly upon the formation of Fe^{3+} ions.

In vitro antibacterial efficacy

The successful demonstration of the efficient *in situ* ROS generation and its upregulation prompted us to assess the antimicrobial properties *in vitro*. To comprehensively evaluate the broad spectrum of activity against both Gram-positive and Gram-negative strains, we employed *Staphylococcus aureus* (*S. aureus*) and *Escherichia coli* (*E. coli*) strains. Furthermore, to evaluate the efficacy of our hydrogel system against drug resistant bacteria, we performed an antibacterial assay against vancomycin-resistant enterococci (Fig. 5C). We cultured the bacterial strains in the presence of H_2O_2 as a control and H_2O_2 with **1$_{GMP}$**. The efficiency of the Fenton reaction was evaluated by culturing **Fe-1$_{GMP}$** with H_2O_2 and **Fe-1$_{GMP}$** with H_2O_2 + AA for 16 hours on agar plates. Fig. 5A–C show substantial growth of bacterial colonies for the control sample with H_2O_2 and the **1$_{GMP}$** hydrogel with H_2O_2, indicating no significant bacterial killing in these samples. Remarkably, we observed a significant decrease in bacterial colony growth for **Fe-1$_{GMP}$** with H_2O_2 for all the three bacterial strains. It is noteworthy that the clinical standard for disinfecting wounds typically involves the use of 3% **H_2O_2**.[54] In our study, we opted for a lower concentration (0.5%) of **H_2O_2** for bacterial killing. Furthermore, we quantified the antimicrobial efficacy by calculating the c.f.u per mL (Fig. 5D).[55] Interestingly, we found 100% killing of the bacterial strains with **Fe-1$_{GMP}$** with H_2O_2 + **AA** as compared to the

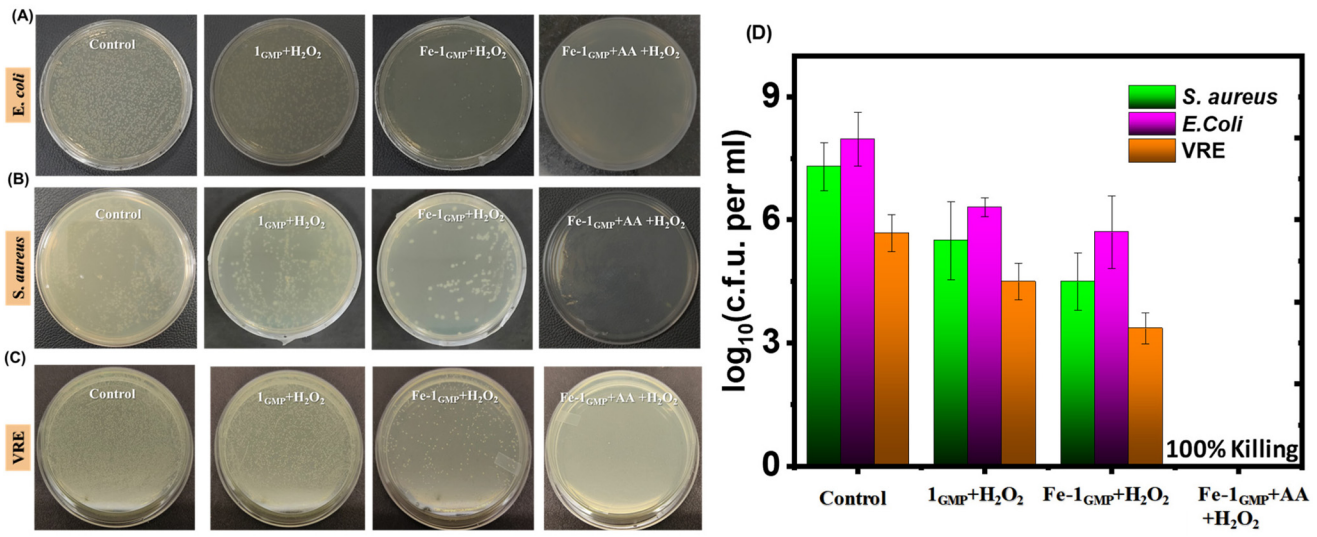

Fig. 5 Images showing the growth of bacterial colonies of (A) *E. coli* (upper panel), (B) *S. aureus* (middle panel) and (C) vancomycin-resistant enterococci (VRE) bacterial strains (lower panel) for the control samples (only H_2O_2) and treated samples of the **1$_{GMP}$** hydrogel with H_2O_2, the **Fe-1$_{GMP}$** hydrogel with H_2O_2 and the AA-loaded **Fe-1$_{GMP}$** hydrogel with H_2O_2. (D) The corresponding quantitative colony forming unit (c.f.u) per mL of *S. aureus*, *E. coli* and the resistant strain of VRE.

other controls: only H_2O_2, $\mathbf{1_{GMP}}$ with H_2O_2 and $\mathbf{Fe\text{-}1_{GMP}}$ with H_2O_2 (Fig. 5D). These observations underscore the efficient antibacterial efficacy of the $\mathbf{Fe\text{-}1_{GMP}}$ hydrogel *via* ROS generation and its upregulation by addition of ascorbic acid, thereby highlighting its potential for antimicrobial applications. Furthermore, we compared our hydrogel system with a broad spectrum topical antibiotic drug, silver sulfadiazine, at its minimum inhibitory concentration (MIC), which showed ~50% bacterial killing with both *E. coli* and *S. aureus* strains (Fig S6A and B†).[56] In this regard, the $\mathbf{Fe\text{-}1_{GMP}}$ hydrogel with H_2O_2 + **AA** showed better antibacterial effect as compared to the topical antibiotics. Recently, Gao *et al.* reported enzymatic cascade micro reactors for the production of hydroxyl radicals to test their activity against multi-drug resistant *S. aureus*.[57] Therefore, our iron-complexed hydrogel system exhibited potent antibacterial activity not only against the Gram-positive and Gram-negative bacteria, but also remained effective against the drug-resistant strain of vancomycin-resistant enterococci. Finally, we evaluated the cytotoxicity of the $\mathbf{Fe\text{-}1_{GMP}}$ and $\mathbf{Fe\text{-}1_{GMP}}$ + **AA** hydrogels in the L929 mouse fibroblast cell line. The quantitative evaluation conducted through the MTT assay revealed more than 80% biocompatibility for both $\mathbf{Fe\text{-}1_{GMP}}$ and **AA**-loaded $\mathbf{Fe\text{-}1_{GMP}}$ after a 48 h incubation period (Fig. S6E†).For the control, L929 cells were cultured on a tissue culture plate. The higher survival rate of the cells indicates the biocompatibility of the hydrogel. These findings indicate minimal cytotoxic effects on the mammalian cells, thereby enhancing the potential applicability of the $\mathbf{Fe\text{-}1_{GMP}}$ hydrogel in biomedical settings.

In vivo antibacterial efficacy

Furthermore, we conducted an *in vivo* study on male Balb/c mice with dorsal skin infections caused by *E. coli* to successfully demonstrate the applicability of the hydrogel as a potential antibacterial agent. The mice were induced with neutropenia by dual administration of a cyclophosphamide drug, followed by creation of skin abrasion at the dorsal midline. The wound site was infected with the pathogenic strain of *E. coli* using a band-aid and incubated for 1 day. The mice were divided in four sets and treatment was given using control (only H_2O_2), $\mathbf{1_{GMP}}$ with H_2O_2, $\mathbf{Fe\text{-}1_{GMP}}$ with H_2O_2 and $\mathbf{Fe\text{-}1_{GMP}}$ with H_2O_2 + AA (Fig. 6A). The next day, the mice were sacrificed and the dorsal skin portions were investigated for bacterial growth. Fig. 6B shows the maximum bacterial colonization for the control mice treated with only H_2O_2 and $\mathbf{1_{GMP}}$ with H_2O_2. Interestingly, mice treated with $\mathbf{Fe\text{-}1_{GMP}}$ with H_2O_2 exhibited a significant decrease in bacterial colonization while mice treated with $\mathbf{Fe\text{-}1_{GMP}}$ + **AA** and H_2O_2 showed the highest killing efficiency, thereby successfully demonstrating the antibacterial efficacy of the hydrogel *via* ROS generation.

Furthermore, the bacteria were stained to quantify live and dead cells, employing Syto-9 (green fluorescent nucleic acid stain) and propidium iodide (PI) in a 1 : 1 staining mixture. Fluorescence microscopy images provided insights into the growth of bacterial cells with live cells stained with SYTO-9 and dead cells stained with propidium iodide (PI). The results highlighted the maximum green emission for the control samples (Fig. 6C). However, in the case of **AA**-loaded

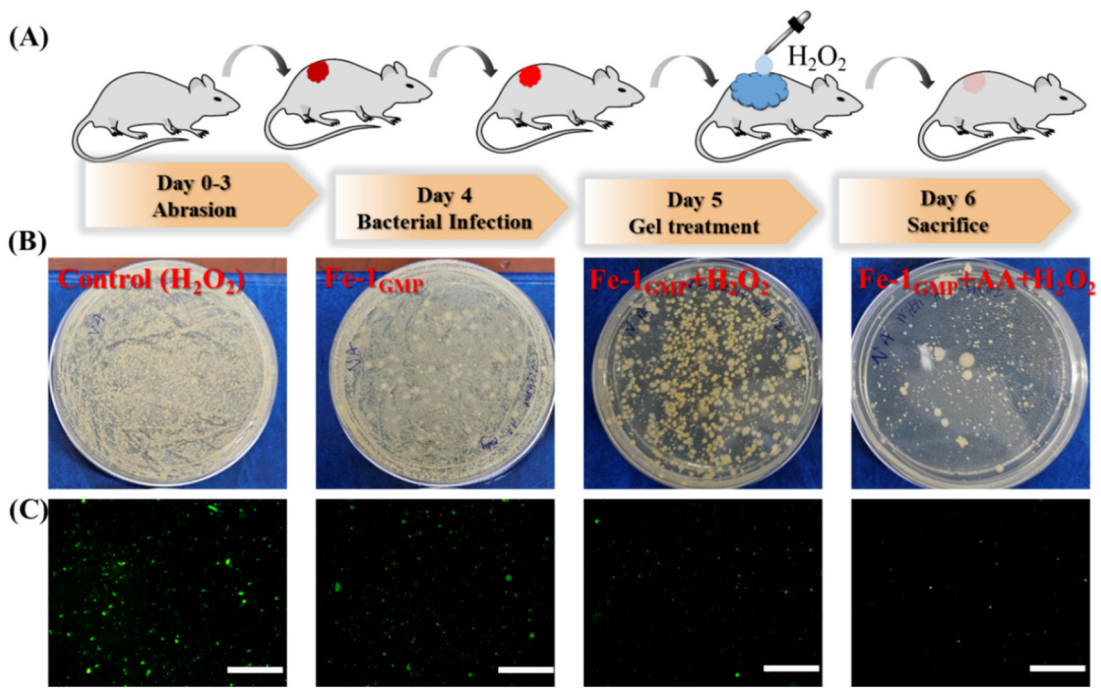

Fig. 6 (A) Schematic illustration showing the detailed day wise protocol for *in vivo* studies on Balb/c mice. (B) Antibacterial activity of $\mathbf{Fe\text{-}1_{GMP}}$ and AA-loaded $\mathbf{Fe\text{-}1_{GMP}}$ showing the growth of bacterial colonization in different samples. (C) Fluorescence microscopy images showing the active bacterial cells emitting green when stained with SYTO-9 dye and the dead cells emitting red when stained with PI.

Fe-1$_{GMP}$ with H_2O_2 treatment, the green fluorescence signal of SYTO-9 was significantly less with a bright red emission from PI signifying the dead bacterial cells. Such a decrease in green fluorescence and an increase in red fluorescence suggest a substantial decrease in the live bacterial cells and enhanced antibacterial properties of the hydrogels *via* ROS generation. Thus, these findings not only supported, but also visually illustrate the potential of the hydrogel for use as an effective antibacterial agent through topical administration to the infected sites.

Conclusions

In conclusion, we have successfully designed an interesting **1$_{GMP}$** hydrogel system based on the extensive hydrogen bonding and stacking interaction between guanosine 5′-monophosphate (GMP) and tetra(4-carboxylphenyl) ethylene (**1**). Extensive characterization through various techniques like ^{1}H-NMR, CD and rheology provided insights into the self-assembly mechanism and mechanical properties of the hydrogels. The hydrogel exhibited tunable aggregation-induced emission properties and mechanical strength upon incorporation of various divalent metal ions such as Ca^{2+}, Mg^{2+} and Fe^{2+} to form mechanically stiffer hydrogels of **M-1$_{GMP}$**. Furthermore, the **Fe-1$_{GMP}$** metallogel was investigated for the *in situ* generation of reactive oxygen species *via* the Fenton reaction that was upregulated upon addition of ascorbic acid. Taken together, the hydrogel's capacity to generate hydroxyl radicals was demonstrated along with its reformability and thixotropic nature to enhance its versatility. Furthermore, owing to such ROS generation, **Fe-1$_{GMP}$** exhibited efficient *in vitro* antibacterial properties against *E. coli*, *S. aureus* and vancomycin-resistant enterococci. Notably, the **Fe-1$_{GMP}$** hydrogel loaded with ascorbic acid exhibited the highest killing efficiency. Finally, *in vivo* experiments on mice with dorsal skin infections validated further **Fe-1$_{GMP}$** hydrogel's antibacterial efficacy, underscoring its potential for topical applications. Such supramolecular metallogels hosting the Fenton chemistry with precise control over the spatiotemporal generation of ROS and adjustable mechanical properties make them suitable for exploitation in bacterial control in wound management in biomedical fields, and work is currently underway in our laboratory toward these applications.

Data availability

The data supporting this article have been included as part of the ESI.†

Conflicts of interest

There are no conflicts to declare.

Acknowledgements

The authors are thankful to the Institute of Nano Science and Technology (INST), Mohali, for providing infrastructure and characterization facilities. The authors are grateful to the animal facilities of IACS, Kolkata. The authors gratefully acknowledge the generous help of Prof. Avinash Bajaj and Varsha Saini from the Regional Centre for Biotechnology (RCB), Faridabad, for providing access to the BSL-II facility to conduct *in vitro* antimicrobial assays of drug-resistant bacteria. SB acknowledges DST for the award of the J C Bose Fellowship. A. Pal expresses gratitude for financial support from SERB grants (CRG/2020/004251) and the Department of Biotechnology (BIRAC-PACE, BT/AIR01159/PACE-21/20). VC and Umesh thank INST for the fellowship.

References

1 H. C. Neu, *Science*, 1992, **257**, 1064–1073.
2 H. Liu, T. Xu, Z. Xue, M. Huang, T. Wang, M. Zhang, R. Yang and Y. Guo, *ACS Infect. Dis.*, 2024, **2**, 350–370.
3 X. Li, S. M. Robinson, A. Gupta, K. Saha, Z. Jiang, D. F. Moyano, A. Sahar, M. A. Riley and V. M. Rotello, *ACS Nano*, 2014, **8**, 10682–10686.
4 K. M. G. O'Connell, J. T. Hodgkinson, H. F. Sore, M. Welch, G. P. C. Salmond and D. R. Spring, *Angew. Chem., Int. Ed.*, 2013, **52**, 10706–10733.
5 Q. Zeng, X. Qi, G. Shi, M. Zhang and H. Haick, *ACS Nano*, 2022, **16**, 1708–1733.
6 Y. Yang, B. Chu, J. Cheng, J. Tang, B. Song, H. Wang and Y. Yao, *Nat. Commun.*, 2022, **13**, 1255.
7 M. K. Pradhan, D. Gupta, K. R. Namdev, C. Miglani, A. Pal and A. Srivastava, *Nanoscale*, 2022, **14**, 15079–15090.
8 L. Schnaider, S. Brahmachari, N. W. Schmidt, B. Mensa, S. Shaham-Niv, D. Bychenko, L. Adler-Abramovich, L. J. W. Shimon, S. Kolusheva, W. F. DeGrado and E. Gazit, *Nat. Commun.*, 2017, **8**, 1365.
9 D. Nath, J. Ralhan, J. P. Joseph, C. Miglani and A. Pal, *Biomacromolecules*, 2024, **25**, 853–863.
10 E. O. Ogunsona, R. Muthuraj, E. Ojogbo, O. Valerio and T. H. Mekonnen, *Appl. Mater. Today*, 2020, **18**, 100473.
11 V. B. Kumar, M. Lahav and E. Gazit, *J. Mater. Chem. B*, 2024, **12**, 2855–2868.
12 M. Makvandi, C. Y. Wang, E. N. Zare, A. Borzacchiello, L. N. Niu and F. R. Tay, *Adv. Funct. Mater.*, 2020, **30**, 1910021.
13 I. J. Budiarso, N. D. W. Rini, A. Tsalsabila, M. D. Birowosuto and A. Wibowo, *ACS Biomater. Sci. Eng.*, 2023, **9**, 3084–3115.
14 P. Prasad and S. Gupta, *ACS Appl. Bio Mater.*, 2020, **3**, 8271–8285.
15 S. Li, S. Dong, W. Xu, S. Tu, L. Yan, C. Zhao, J. Ding and X. Chen, *Adv. Sci.*, 2018, **5**, 1700527.
16 B. O. Okesola and D. K. Smith, *Chem. Soc. Rev.*, 2016, **45**, 4226–4251.

17 M. C. Sardaru, S. Morariu, O. E. Carp, E. L. Ursu, A. Rotaru and M. Barboiu, *Chem. Commun.*, 2023, **59**, 3134–3137.
18 A. Maleki, J. He, S. Bochani, V. Nosrati, M. A. Shahbazi and B. Guo, *ACS Nano*, 2021, **15**, 18895–18930.
19 S. Ghosh, S. Mukherjee, D. Patra and J. Haldar, *Biomacromolecules*, 2022, **23**, 592–608.
20 K. Ghosal, D. Chakraborty, V. Roychowdhury, S. Ghosh and S. Dutta, *ACS Omega*, 2022, **7**, 43364–43380.
21 Z. Ahmadian, A. Correia, M. Hasany, P. Figueiredo, F. Dobakhti, M. R. Eskandari, S. H. Hosseini, R. Abiri, S. Khorshid, J. Hirvonen, H. A. Santos and M.-A. Shahbazi, *Adv. Healthcare Mater.*, 2021, **10**, 2001122.
22 B. Bhattacharjee, S. Ghosh and J. Haldar, *ACS Appl. Bio Mater.*, 2023, **6**, 4867–4876.
23 S. Kumar, S. Pal, J. Thakur, P. Rani, K. Rana, A. Kar, R. Kar, D. Mehta, S. K. Jha, M. K. Pradhan, D. Jain, K. Rajput, S. Mishra, M. Ganguli, A. Srivastava, U. Dasgupta, V. S. Patil and A. Bajaj, *ACS Appl. Mater. Interfaces*, 2021, **13**, 44041–44045.
24 S. Paul, S. Verma and Y.-C. Chen, *ACS Infect. Dis.*, 2024, **10**, 1034–1055.
25 M. Halder, M. Narula and Y. Singh, *Bioconjugate Chem.*, 2023, **34**, 645–663.
26 I. Mukherjee, A. Ghosh, P. Bhadury and P. De, *ACS Omega*, 2017, **2**, 1633–1644.
27 V. Castelletto, R. H. Barnes, K. A. Karatzas, C. J. Edwards-Gayle, F. Greco, I. W. Hamley, R. Rambo, J. Seitsonen and J. Ruokolainen, *Biomacromolecules*, 2018, **19**, 2782–2794.
28 G. Pandit, N. Chowdhury, Sk. A. Mohid, A. P. Bidkar, A. Bhunia and S. Chatterjee, *ChemMedChem*, 2021, **16**, 355–367.
29 E. Pazos, E. Sleep, C. M. Rubert Pérez, S. S. Lee, F. Tantakitti and S. I. Stupp, *J. Am. Chem. Soc.*, 2016, **138**, 5507–5510.
30 J. Ralhan, V. Kumar, H. Bhatt, D. Nath, N. A. Mavlankar, H. N. Ghosh and A. Pal, *Langmuir*, 2024, **5**, 2754–2763.
31 A. M. Itoo, M. Paul, S. G. Padaga, B. Ghosh and S. Biswas, *ACS Omega*, 2022, **7**, 45882–458909.
32 S. Liao, M. Cai, R. Zhu, T. Fu, Y. Du, J. Kong, Y. Zhang, C. Qu, X. Dong, J. Ni and X. Yin, *Mol. Pharmaceutics*, 2023, **20**, 875–885.
33 S. D. Bhagat and A. Srivastava, *Biomater. Sci.*, 2020, **8**, 4750–4756.
34 X. Wang and M. Zheng, *ACS Appl. Nano Mater.*, 2023, **6**, 13689–13697.
35 B. Yang, Y. Chen and J. Shi, *Chem. Rev.*, 2019, **119**, 4881–4985.
36 H. Ranji-Burachaloo, P. A. Gurr, D. E. Dunstan and G. G. Qiao, *ACS Nano*, 2018, **12**, 11819–11837.
37 Z. Tang, P. Zhao, H. Wang, Y. Liu and W. Bu, *Chem. Rev.*, 2021, **121**, 1981–2019.
38 S. Ghosh, A. Maity and N. R. Jana, *ACS Appl. Nano Mater.*, 2023, **6**, 21595–21602.
39 I. Banerjee, R. C. Pangule and R. S. Kane, *Adv. Mater.*, 2011, **23**, 690–718.
40 M. Godoy-Gallardo, M. Merino-Gómez, L. C. Matiz, M. A. Mateos-Timoneda, F. J. Gil and R. A. Perez, *ACS Biomater. Sci. Eng.*, 2022, **9**, 40–61.
41 V. D. Nguyen, A. Pal, F. Snijkers, M. Colob-Delsuc, G. Leonetti, S. Otto and J. van der Gucht, *Soft Matter*, 2016, **12**, 432–440.
42 A. Singh, J. P. Joseph, D. Gupta, C. Miglani, N. A. Mavlankar and A. Pal, *Nanoscale*, 2021, **13**, 13401–13409.
43 E. Mattia, A. Pal, G. Leonetti and S. Otto, *Synlett*, 2017, **28**, 103–107.
44 C. Zheng, X. Wu, M. Liu, Y. Lan, Q. Liu, E. Cai, Z. Liao and J. Shen, *Smart Med.*, 2024, e20230047.
45 G. M. Peters, L. P. Skala, T. N. Plank, H. Oh, G. N. M. Reddy, A. Marsh, S. P. Brown, S. R. Raghavan and J. T. Davis, *J. Am. Chem. Soc.*, 2015, **137**, 5819–5827.
46 S. Sarkar, S. Bera, P. Moitra and S. Bhattacharya, *Mater. Today Chem.*, 2023, **30**, 101554.
47 A. Bhunia, V. Vasylyeva and C. Janiak, *Chem. Commun.*, 2013, **49**, 3961–3963.
48 D. Bhattacharyya, G. M. Arachchilage and S. Basu, *Front. Chem.*, 2016, **4**, 38.
49 H. X. Jiang, Y. Cui, T. Zhao, H. W. Fu, D. Koirala, J. A. Punnoose, D. M. Kong and H. Mao, *Sci. Rep.*, 2015, **5**, 9255.
50 A. Ghosh, B. Parasar, T. Bhattacharyya and J. Dash, *Chem. Commun.*, 2016, **52**, 11159–11162.
51 J. P. Joseph, N. Gupta, C. Miglani, D. Nath, A. Singh, D. Gupta and A. Pal, *Chem. Mater.*, 2022, **34**, 4364–4374.
52 J. Thomas, N. Gupta, J. P. Joseph, V. Chopra, A. Pal and D. Ghosh, *ACS Biomater. Sci. Eng.*, 2021, **7**, 5798–5809.
53 K. Sharma, J. P. Joseph, A. Sahu, N. Yadav, M. Tyagi, A. Singh, A. Pal and K. P. R. Kartha, *RSC. Adv.*, 2019, **9**, 19819–19827.
54 G. Zhu, Q. Wang, S. Lu and Y. Niu, *Med. Princ. Pract.*, 2017, **26**, 301–308.
55 F. A. Pinho-Ribeiro, L. Deng, D. V. Neel, O. Erdogan, H. Basu, D. Yang, S. Choi, A. J. Walker, S. Carneiro-Nascimento, K. He and G. Wu, *Nature*, 2023, **615**, 472–481.
56 G. Sandri, M. C. Bonferoni, F. D'Autilia, S. Rossi, F. Ferrari, P. Grisoli, M. Sorrenti, L. Catenacci, C. Del Fante, C. Perotti and C. Caramella, *Eur. J. Pharm. Biopharm.*, 2013, **84**, 84–90.
57 T. Li, J. Li, Q. Pang, L. Ma, W. Tong and C. Gao, *ACS Appl. Mater. Interfaces*, 2019, **11**, 6789–6795.

